Journal of Power Sources 295 (2015) 9–15

Contents lists available at ScienceDirect

Journal of Power Sources

journal homepage: www.elsevier.com/locate/jpowsour

# Electrochemical properties of MnS–C and MnO–C composite powders prepared via spray drying process

Kyung Min Jeon, Jung Sang Cho, Yun Chan Kang*

*Department of Materials Science and Engineering, Korea University, Anam-Dong, Seongbuk-Gu, Seoul, 136-713, Republic of Korea*

## HIGHLIGHTS

- Spherical MnS–C and MnO–C composite powders are prepared by spray drying process.
- Dextrin plays a key role in the preparation of MnS–C and MnO–C composite powders.
- MnS–C powders exhibit good electrochemical properties for lithium-ion storage.

## GRAPHICAL ABSTRACT

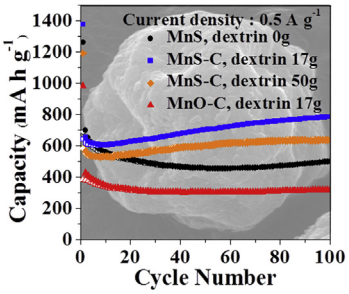


## ARTICLE INFO

*Article history:*
Received 30 March 2015
Received in revised form
4 June 2015
Accepted 28 June 2015
Available online 7 July 2015

*Keywords:*
Energy storage materials
Energy conversion
Carbon composite
Manganese sulfide
Spray drying

## ABSTRACT

Spherical micron-sized MnS–C and MnO–C composite powders are successfully prepared by post-treating the spray-dried precursor powders. Dextrin, which is used as the carbon source material, plays a key role in the preparation of the composite powders with regular morphologies; the bare MnS and MnO powders prepared from the spray solution without dextrin have irregular morphologies. The MnS–C composite powders prepared from the spray solution containing 17 g $L^{-1}$ of dextrin have mixed crystal structures of α- and γ-MnS phases. These powders exhibit superior electrochemical properties compared with those of their MnS and MnO–C counterparts. For example, at a current density of 0.5 A $g^{-1}$, the MnO–C powders have a 100th-cycle discharge capacity of 321 mA h $g^{-1}$; the corresponding discharge capacities of the MnS powders prepared from spray solutions containing 0, 17, and 50 g $L^{-1}$ of dextrin are 501, 786, and 636 mA h $g^{-1}$, respectively.



## 1. Introduction

Metal sulfide materials have been widely used as anode materials for lithium-ion batteries (LIBs) [1–12]. Several studies have been conducted, particularly on the metal sulfide-carbon composite powders, with the aim of improving the electrochemical properties of metal sulfides [13–32]. For example, the inclusion of carbon materials improves the structural stability of these metal sulfides during cycling and augments the conductance of the active materials [16–18]. Control of the morphology and mean size of the metal sulfide and metal sulfide-carbon composite materials is, however, essential to their efficient application in LIBs. Spherical micron-sized powders have been successfully applied as anode materials for LIBs owing to their high packing density on the current collector [33,34]. However, the efficient large-scale production of spherical micron-sized metal sulfide-carbon composite materials with suitable structures for application in LIBs has been scarcely studied.

* Corresponding author.
*E-mail address:* yckang@korea.ac.kr (Y.C. Kang).

http://dx.doi.org/10.1016/j.jpowsour.2015.06.142
0378-7753/

The spray drying process was developed for the large-scale production of spherical micron-sized metal oxide and metal oxide-carbon composite powders [35–48]. However, direct sulfidation of the metal oxide powders could not be performed owing to the low preparation temperature of this process; therefore, metal sulfide materials have been rarely prepared via the spray drying process. In addition, compared with their SnS–C, NiS–C, $MoS_2$–C, and $CoS_x$–C counterparts, significantly fewer studies have been conducted on the MnS–C composite materials [19–32]. Therefore, in this study, micron-sized manganese salt-dextrin composite powders with spherical shapes were prepared via a pilot-scale spray drying process; i.e., MnS–C composite powders were prepared by post-treating the spray-dried precursor powders under an $H_2S$ atmosphere. Moreover, the effect of the dextrin content of the spray solution on the morphological and electrochemical properties of these powders was investigated. These electrochemical properties were compared with those of the MnO–C composite powders prepared by the same process but without applying the sulfur source material.

## 2. Experimental

### 2.1. Synthesis of MnS–C and MnO–C composite powders

The pilot-scale spray drying system that was used to prepare a spray-dried dense powder composed of spherical particles is shown in Fig. S1. The temperatures at the inlet and outlet of the spray dryer were fixed at 300 °C and 120 °C, respectively, and a two-fluid nozzle was used as an atomizer; the atomization pressure was 2.0 bar. The precursor solution for spray drying (i.e., the spray solution) was prepared by dissolving 0.15 M manganese acetate tetrahydrate [$Mn(CH_3COO)_2 \cdot 4H_2O$, Junsei] and 17 and 50 g $L^{-1}$ of dextrin [$(C_6H_{10}O_5)_n$, Samchun] in distilled water. Furthermore, MnO and MnO–C composite powders were obtained by post-treating the spray-dried precursor powders in Ar; i.e., the precursor powders were heated at a rate of 5 °C $min^{-1}$ to 300 °C and then maintained at that temperature for 3 h. MnS and MnS–C powders were subsequently obtained by sulfiding the respective MnO and MnO–C powders at 300 °C for 12 h under a 10% $H_2$/Ar gas atmosphere, with thiourea as the sulfur source. An alumina boat containing the MnO or MnO–C powders was placed in a larger alumina boat with a cover. A thiourea powder was then loaded on the outside of the small alumina boat for complete sulfidation of the powders. The hydrogen sulfide gas, which is required for the sulfidation, was produced through decomposition of the melted thiourea under the $H_2$/Ar carrier gas.

### 2.2. Characterization

The crystal structures of the powders were determined from X-ray diffraction (XRD, Rigaku DMAX-33) measurements, which were performed at the Korea Basic Science Institute in Daegu. The corresponding morphological characteristics were examined using a scanning electron microscope (SEM, TESCAN VEGA3 SBH) and high-resolution transmission electron microscope (TEM, JEOL JEM-2010). The specific surface areas of the powders were calculated from a Brunauer–Emmett–Teller (BET) analysis of the nitrogen adsorption measurements (TriStar 3000). The MnO–C and MnS–C composite powders were investigated using X-ray photoelectron spectroscopy (XPS, ESCALAB-210) with Al Ka radiation (1486.6 eV). In addition, the decomposition characteristics of the precursor powder were determined via thermogravimetric analysis (TGA, SDT Q600), which was performed in air at a heating rate of 10 °C $min^{-1}$.

### 2.3. Electrochemical measurements

The capacities and cycle properties of the powders were determined in 2032-type coin cells whose electrodes were prepared from a mixture containing 70 wt% active material, 20 wt% Super P, and 10 wt% sodium carboxymethyl cellulose binder. Lithium metal and microporous polypropylene film were used as the counter electrode and separator, respectively. A 1 M $LiPF_6$ solution in a 1:1 mixture (by volume) of ethylene carbonate/dimethyl carbonate with 5% fluoroethylene carbonate was used as the electrolyte. The charge/discharge characteristics of the samples were determined by cycling in the 0.001–3 V potential range at a set of fixed current densities and the corresponding cyclic voltammetry (CV) measurements were performed at a scan rate of 0.07 mV $s^{-1}$. The size of the negative electrode was 1 cm × 1 cm and the mass loading of active material was approximately 1.0 mg $cm^{-2}$.

## 3. Results and discussion

The morphologies of the precursor powders prepared via spray drying from the spray solutions with and without dextrin are shown in Fig. 1. Owing to the low hygroscopicity of the salt, the manganese acetate-containing droplets were well-dried (Fig. 1), and hence exhibited non-aggregation characteristics, irrespective of the dextrin content. This rapid drying resulted however, in spherical powders, which have a pork-marked structure. MnS powders were produced by post-treating the precursor powders via a two-step process; i.e., the precursor powders were heated under Ar atmosphere for 3 h (first step) and then sulfidated under 10% $H_2$/Ar atmosphere for 12 h (second step). The XRD pattern (Fig. 2) reveals that the first-step post-treated powders have a phase-pure MnO crystal structure. Moreover, the amorphous carbon resulting from the carbonization of dextrin under Ar atmosphere led in turn, to the formation of MnO–C composite powders from the dextrin-containing spray solution. For dextrin contents of 0 and 17 g $L^{-1}$, these powders have mean crystallite sizes of 18 and 10 nm, respectively, as calculated from the (200) peak widths using Scherrer's equation. The XRD pattern of the MnO–C composite powders prepared from spray solutions containing 50 g $L^{-1}$ of dextrin exhibited no XRD peaks, which correspond solely to the amorphous phases. The amorphous carbon retarded the crystal growth of the MnO phase during the post-treatment process. The XRD patterns of the powders obtained after sulfidation process had phase pure crystal structure of MnS. In other words, MnS and MnS–C powders resulted from the sulfidation of the MnO and MnO–C powders, respectively. The bare MnS powders have a phase-pure α-MnS crystal structure. On the other hand, the MnS–C composite powders prepared from the spray solution containing 17 g $L^{-1}$ of dextrin had a mixed crystal structure of α- and γ-MnS phases. The XRD pattern shows, however, that the MnS–C composite powders prepared from the spray solution containing 50 g $L^{-1}$ of dextrin have an amorphous-like structure. XPS analysis was performed to confirm the accurate phase of the MnO–C and MnS–C composite powders prepared from the spray solution containing 50 g $L^{-1}$ of dextrin. In the case of MnO–C, the main peaks observed in the XPS spectrum were O1s with peak locating at 531.4 eV and Mn2p with two peaks locating at 641.5 eV for $Mn2p_{3/2}$ and 653.2 eV for $Mn2p_{1/2}$, which are the characteristics of MnO [49,50]. In the case of MnS–C, the S2p peak at 160.9 eV was observed in the XPS spectrum along with the peaks for $Mn2p_{3/2}$ and $Mn2p_{1/2}$, which are consistent with the reference value of MnS [51,52]. The MnS powders prepared from the spray solutions with dextrin contents of 0 and 17 g $L^{-1}$ have mean crystallite sizes of 19 and 17 nm, respectively, as calculated from the (200) peak widths using Scherrer's equation. Fig. 3 shows the TG curves of the MnO–C,

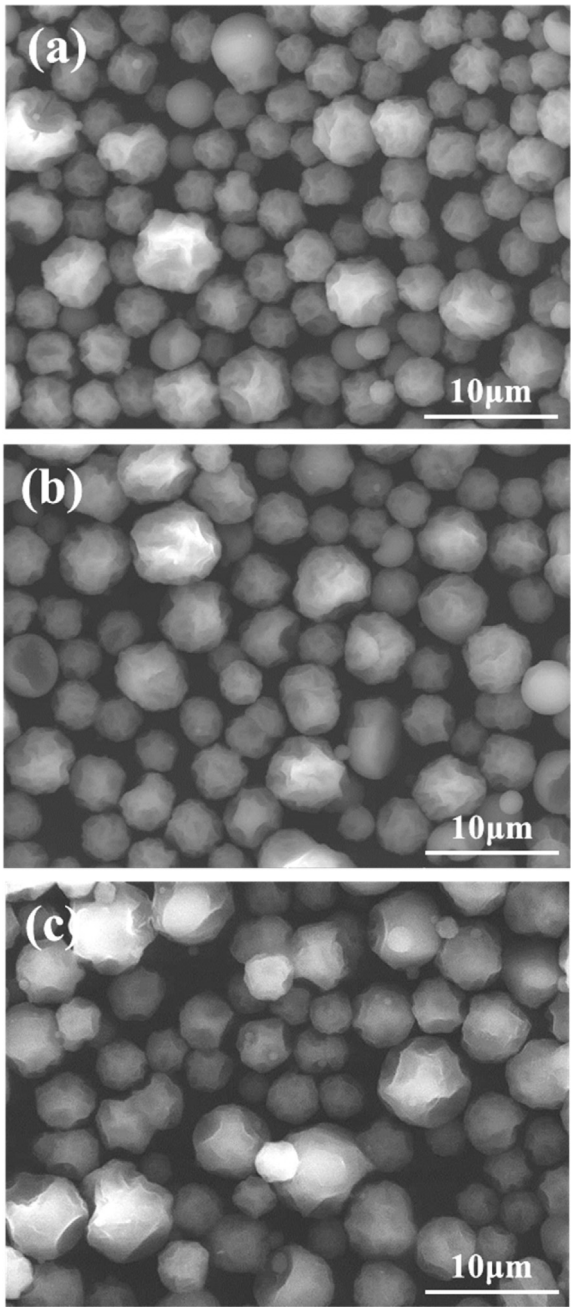


**Fig. 1.** Morphologies of the precursor powders prepared by spray drying process: (a) dextrin 0 g, (b) dextrin 17 g, and (c) dextrin 50 g.

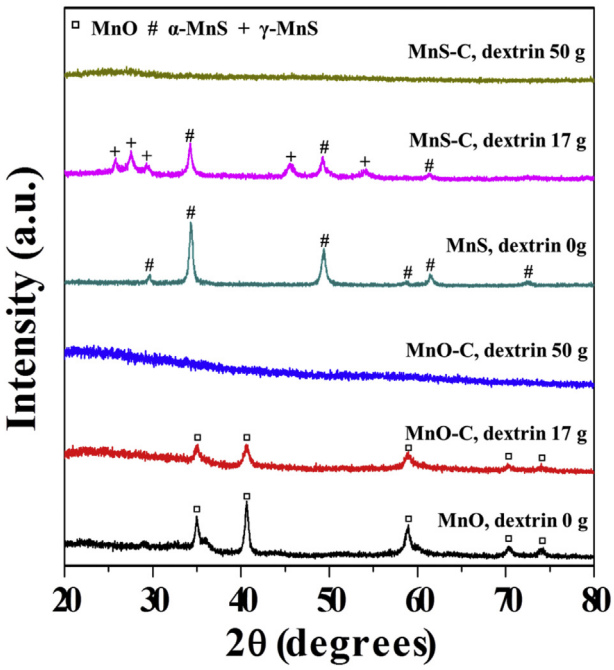


**Fig. 2.** XRD patterns of the MnO, MnS, MnO–C, and MnS–C powders.

MnS, and MnS–C powders. The TG curve of the MnO–C composite powders prepared from the spray solution containing 17 g $L^{-1}$ of dextrin exhibits a two-step weight loss for temperatures of up to 900 °C as shown in Fig. 3a. The first step, which occurs at temperatures below 200 °C, is associated with the loss of water adsorbed on the MnO–C composite powders. The abrupt weight loss at ~200 °C (i.e., the second step) is attributed to the composition of amorphous carbon. However, the weight increase stemming from the oxidation of MnO into $Mn_2O_3$ results in a slight decrease in the weight loss associated with the combustion of amorphous carbon. The TG curve of the bare MnS powders shown in Fig. 3b reveals three-step weight loss and one-step weight increase for temperatures below 900 °C. The second and third step losses result from the conversion of MnS into $Mn_2O_3$ via $Mn_3O_4$ and $MnSO_4$ intermediates. The weight increase stemming from the conversion reaction of MnS into $MnSO_4$ results in a slight decrease in the weight loss associated with the oxidation of MnS at ~500 °C. The third step of the weight loss, which occurs at ~715 °C is attributed to the decomposition of $MnSO_4$ and oxidation of $Mn_3O_4$ into $Mn_2O_3$. The TG curves of the MnS–C composite powders prepared from the spray solutions containing 17 and 50 g $L^{-1}$ of dextrin also reveal three-step weight loss for temperatures below 900 °C. The abrupt weight loss at ~400 °C (i.e., the second step) is attributed to the combustion of amorphous carbon. Moreover, sulfidation of the composite powders resulted in an increasing of the combustion temperature of the carbon material. The weight increase stemming from the conversion reaction of MnS into $Mn_3O_4$ and $MnSO_4$ results in a slight decrease in the weight loss associated with the combustion of amorphous carbon. However, oxidation of some amount of $Mn_3O_4$ and $MnSO_4$ intermediates occur by heat evolution by combustion of carbon material. Therefore, the weight loss by conversion of $MnSO_4$ into $Mn_2O_3$ was low in the third step weight loss at ~715 °C. Carbon contents of 41, 47, and 61% were estimated from the TG analysis of the MnO–C, MnS–C, and MnS–C composite powders prepared from the spray solutions containing 17, 17, and 50 g $L^{-1}$ of dextrin respectively.

The morphologies of the bare MnO and MnO–C powders are shown in Fig. S3. The particles of the bare MnO powders have irregular shapes and a broad distribution of sizes. Furthermore, owing to their low melting temperature (210 °C), the spherical manganese acetate powders formed via the spray drying process melted before being decomposed into MnO powders. However, dextrin, which was used as the carbon source material, prevented the deformation of these spherical powders during the formation of the MnO–C composite powders. The MnO–C composite powders have, therefore, similar shape to that of the spray-dried powders, which have a pork-marked structure. The BET surface area of the MnO–C powders prepared from the spray solution containing 17 g $L^{-1}$ of dextrin was 0.6 $m^2$ $g^{-1}$. The SEM images (Figs. S3 and 4) reveal the similarities between the morphologies of the powders

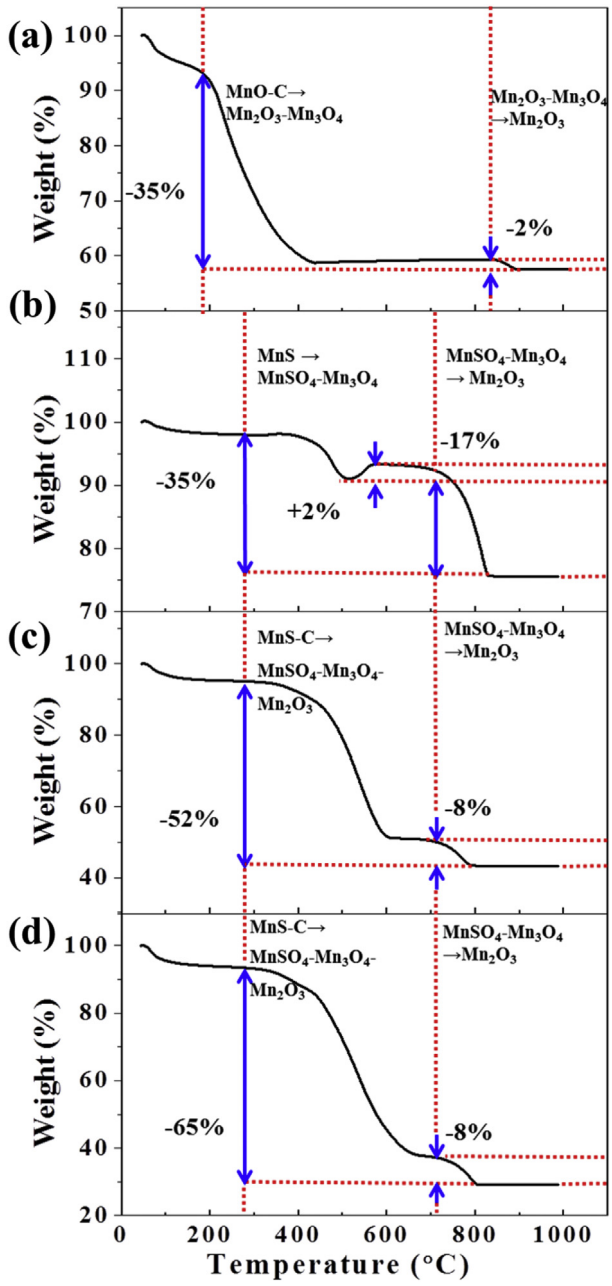


**Fig. 3.** TG curves of the MnO–C, MnS, and MnS–C powders: (a) MnO–C, dextrin 17 g, (b) MnS, dexrtin 0 g, (c) MnS–C, dextrin 17 g, and (d) MnS–C, dextrin 50 g.

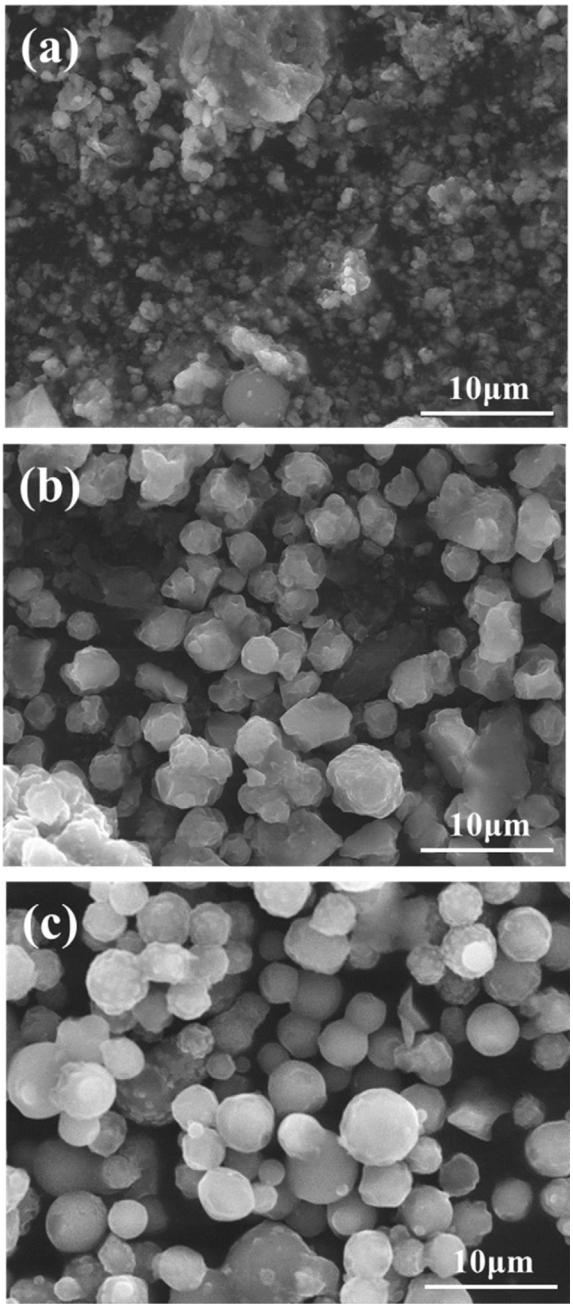


**Fig. 4.** Morphologies of the MnS and MnS–C powders: (a) dextrin 0 g, (b) dextrin17 g, and (c) dextrin 50 g.

obtained before and after the sulfidation process; i.e., the spherical morphology and non-aggregation characteristics of the MnO–C composite powders were retained even after complete sulfidation at 300 °C. The bare MnS powders had smaller size than those of the MnS–C composite powders as shown in Fig. 4. The MnS–C composite powders prepared from the spray solution containing 17 g $L^{-1}$ of dextrin have a mean size of 3.9 μm. High resolution SEM and TEM images and elemental mapping images (Fig. 5) also reveal their filled structure and rough surface. In fact, the high-resolution TEM image shown in Fig. 5c shows a well-faceted nanocrystal that is uniformly covered with amorphous carbon. The inset image in Fig. 5c also shows the clear 0.32 nm-spaced lattice fringes, corresponding to the (002) crystal plane of γ-MnS. The elemental mapping images shown in Fig. 5d reveal the uniform distributions of Mn, S, and C components all over the MnS–C composite powder. The BET surface areas of the MnS powders prepared from the spray solutions containing 0, 17, and 50 g $L^{-1}$ of dextrin were 11.1, 2.3, and 1.5 $m^2$ $g^{-1}$, respectively.

The electrochemical properties of the MnS, MnO–C, and MnS–C powders are shown in Figs. 6 and 7. Fig. 6a–c shows the cyclic voltammetry (CV) curves for the first 5 cycles, which were obtained at a scan rate of 0.07 mV $s^{-1}$ in the potential range of 0.001–3.0 V. The peaks near 0.39 and 0.28 V in the CV curves of the bare MnS and MnS–C powders, respectively, are attributed to the reduction of MnS to metallic Mn and the formation of amorphous $Li_2O$ [10–12,19–21]. However, the ultrafine MnS crystallites in the MnS–C composite powders resulted in an unclear reduction peak in the initial discharge process. The reduction peak at ~0.05 V in the

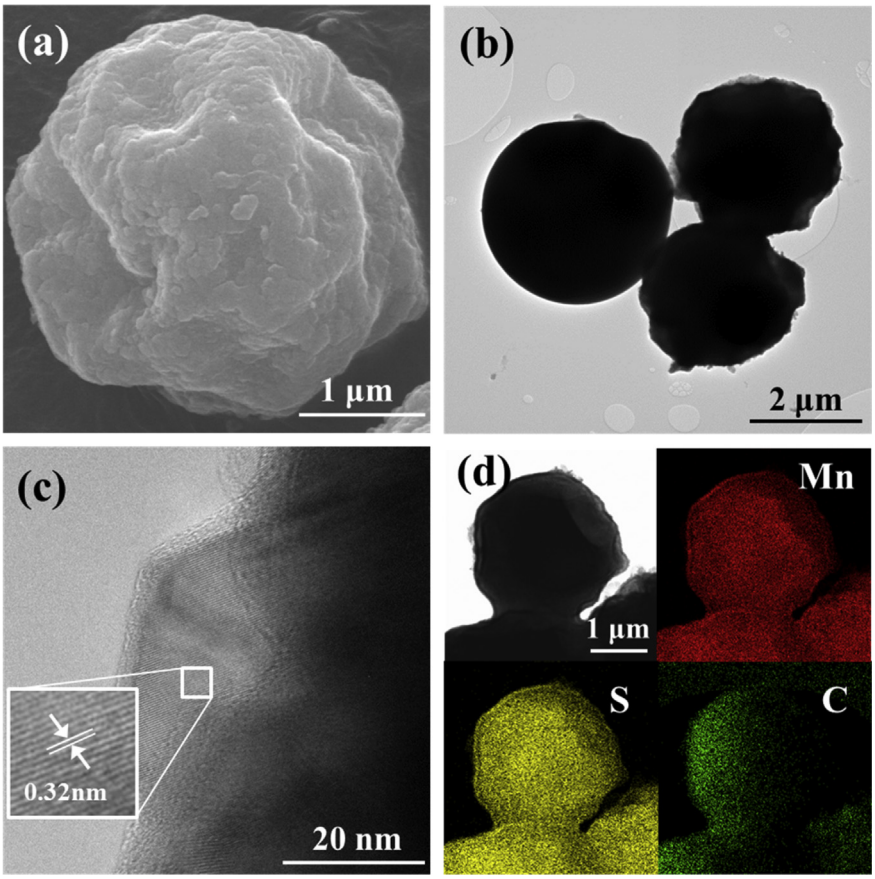


**Fig. 5.** Morphologies and elemental mapping images of the MnS–C powders prepared from the spray solution with 17 g dextrin: (a) high resolution SEM image, (b) low resolution TEM image, (c) high resolution TEM image, and (d) elemental mapping images.

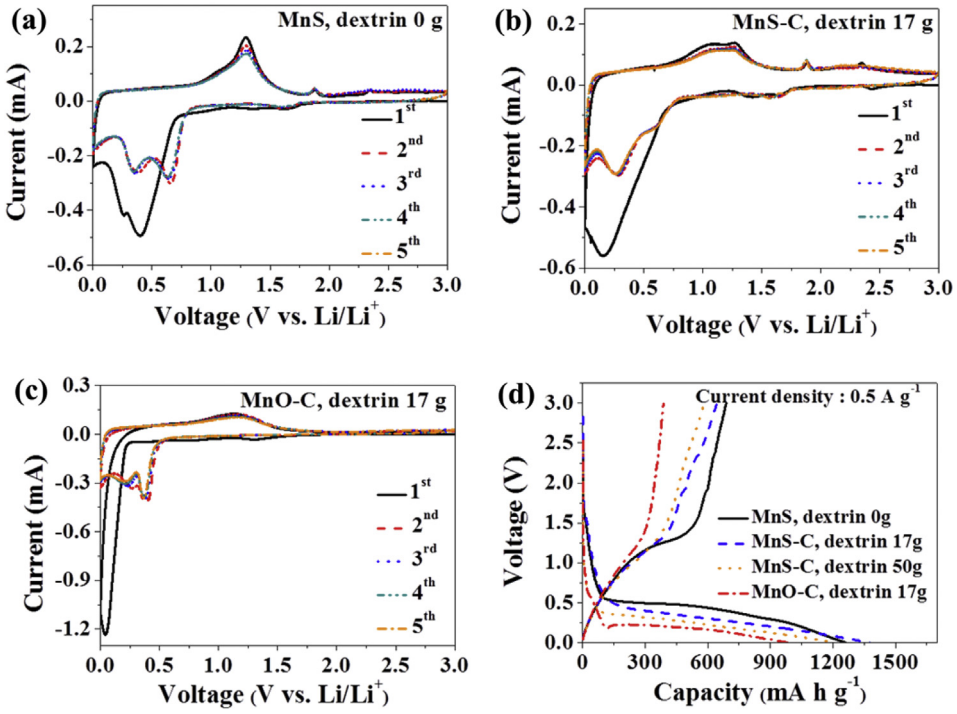


**Fig. 6.** CV curves and initial discharge and charge curves of the powders: CV curves of (a) MnS (dextrin 0 g), (b) MnS–C (dextrin 17 g), (c) MnO–C (dextrin17 g), and (d) initial charge and discharge curves of the MnS, MnS–C, and MnO–C powders.

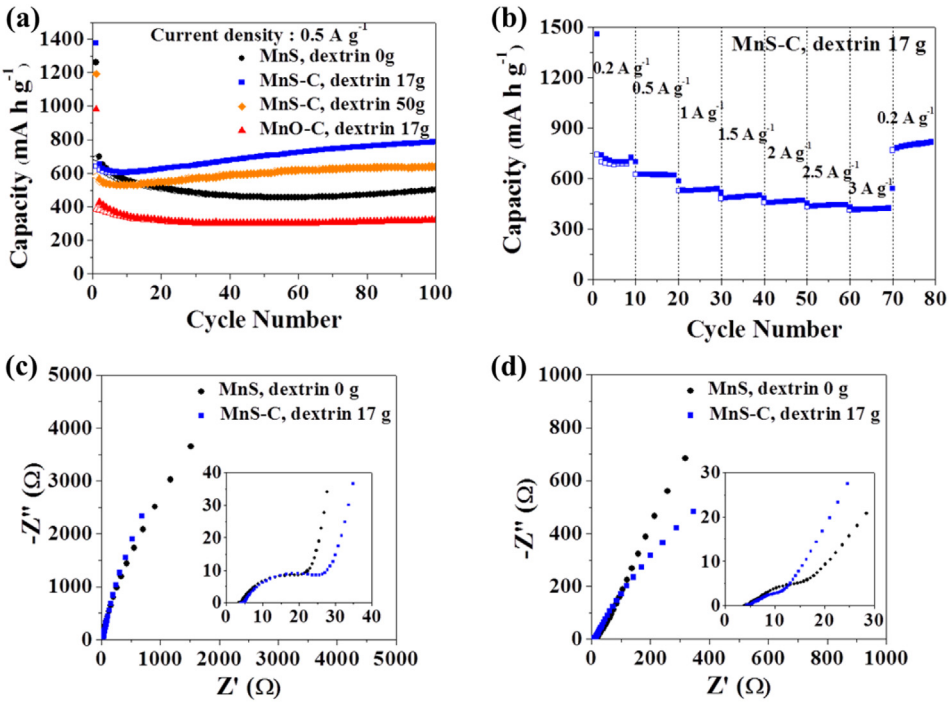


**Fig. 7.** Electrochemical properties of the MnS, MnS–C, and MnO–C powders: (a) cycling performances, (b) rate performance of the MnS–C (dextrin 17 g), (c) Nyquist plots before cycling, and (d) Nyquist plots after 50 cycles.

initial CV curve of the MnO–C powders can be attributed to the reduction of MnO to metallic Mn via the reaction: $MnO + 2\,Li^+ + 2\,e^- \rightarrow Li_2O + Mn$ [53,54]. Fig. 6d shows the initial charge and discharge curves of the MnS, MnO–C, and MnS–C powders at a current density of 0.5 A $g^{-1}$. Owing to their ultrafine crystallite sizes, the plateaus in the initial charge and discharge curves of the MnS–C and MnO–C composite powders were insignificant compared with those of the bare MnS powders. The MnS powders prepared from the spray solutions containing 0, 17, and 50 g $L^{-1}$ of dextrin had initial discharge capacities of 1261, 1378, and 1192 mA h $g^{-1}$, respectively, and corresponding initial Coulombic efficiencies of 54, 47, and 49%. The higher initial Coulombic efficiency of the composite powders prepared from the spray solution containing 50 g $L^{-1}$ of dextrin, compared to that its 17 g $L^{-1}$ counterpart, stems from the higher structural stability of the amorphous-like MnS–C composite powders with high carbon content. Furthermore, the high amount of amorphous carbon with high initial irreversible capacity loss resulted in lower initial Coulombic efficiencies of the MnS–C composite powders compared with that of their bare MnS counterparts. The MnO–C composite powders prepared from the spray solution containing 17 g $L^{-1}$ of dextrin had initial discharge and charge capacities of 984 and 387 mA h $g^{-1}$, respectively.

Fig. 7a shows the cycling performances of the MnS, MnO–C, and MnS–C powders at a current density of 0.5 A $g^{-1}$. The discharge capacities of the bare MnS powders decreased gradually during cycling owing to continuous structural damage. In contrast, the discharge capacities of the MnS–C composite powders decreased only slightly during the first 10 cycles but increased gradually with further cycling, which is attributed to the formation of the solid electrolyte interphase (SEI) during the subsequent charge process. This SEI plays a major role because it can be partially decomposed due to the catalytic activity of metallic nanoparticles [55–58]. The partially reversible formation/decomposition of the SEI will lead to an extra capacity of the cell. The MnS powders prepared from the spray solutions containing 0, 17, and 50 g $L^{-1}$ of dextrin have 100th-cycle discharge capacities of 501, 786, and 636 mA h $g^{-1}$, respectively; the MnO–C powders have a 100th-cycle discharge capacity of 321 mA h $g^{-1}$. The electrode density of the MnS–C composite powders prepared from the spray solution containing 17 g $L^{-1}$ of dextrin was 0.67 g $cm^{-3}$. The volumetric discharge capacity of the MnS–C composite powders prepared from the spray solution containing 17 g $L^{-1}$ of dextrin at the 100th cycle was 524 mA h $cm^{-3}$.

Fig. 7b shows the rate performance of the MnS–C composite powders prepared from the spray solution containing 17 g $L^{-1}$ of dextrin, with the current density increased stepwise from 0.2 to 3 A $g^{-1}$ and with 10 cycles performed at each step. Final discharge capacities of 698, 586, 516, 482, 452, 429, and 423 mA h $g^{-1}$ were obtained at current densities of 0.2, 0.5, 1, 1.5, 2, 2.5, and 3 A $g^{-1}$, respectively. Furthermore, the powders exhibited excellent recovery of the discharge capacity to 817 mA h $g^{-1}$ when the current density was returned to 0.2 A $g^{-1}$ after 70 cycles.

Electrochemical impedance spectroscopy (EIS) measurements were performed on the MnS and MnS–C powders before and after 50 cycles in order to investigate the superior cycling performance of the latter compared to that of the former. The impedance spectra obtained before and after 50 cycles are shown in Fig. 7c and d. The Nyquist plots exhibit compressed semicircles in the medium-frequency range, which is related to the charge-transfer resistance ($R_{ct}$) of the electrode [59,60]. The pre-cycling and 50$^{th}$-cycle charge transfer resistance of the MnS–C composite powders are higher and lower, respectively than that of the bare MnS powders. The structural instability of the bare MnS powders during cycling increased the charge transfer resistance. Based on the aforementioned results, the superior electrochemical properties of the MnS–C powders, compared with those of the bare MnS powders, stem from their structural stability during repeated lithium insertion and desertion processes.

## 4. Conclusions

A spray drying process was applied to the large-scale production of spherical, non-aggregating MnO–C and MnS–C composite powders. The spray-dried composite powders of Mn acetate and dextrin were transformed into the spherical MnO–C composite powders by post-treatment under Ar atmosphere; these powders were, in turn, transformed into spherical MnS–C composite powders via a simple sulfidation process under $H_2S$ gas. The amount of dextrin dissolved in the spray solution affected the crystal structures and morphologies of the MnS powders. Furthermore, the MnS–C composite powders prepared from the spray solution containing 17 g $L^{-1}$ of dextrin exhibited excellent electrochemical properties and are therefore suitable anode materials for LIBs.

## Appendix A. Supplementary data

Supplementary data related to this article can be found at http://dx.doi.org/10.1016/j.jpowsour.2015.06.142.

## References


[1] C. Xu, Y. Zeng, X. Rui, N. Xiao, J. Zhu, W. Zhang, J. Chen, W. Liu, H. Tan, H. HoonHng, Q. Yan, ACS Nano 6 (2012) 4713–4721.
[2] H.S. Hwang, H.J. Kim, J.P. Cho, Nano Lett. 11 (2011) 4826–4830.
[3] S.H. Choi, Y.C. Kang, Small 3 (2014) 474–478.
[4] Q. Wang, L. Jiao, Y. Han, H. Du, W. Peng, Q. Huan, D. Song, Y. Si, Y. Wang, H. Yuan, J. Phys. Chem. C 115 (2011) 8300–8304.
[5] B. Wu, H. Song, J. Zhou, X. Chen, Chem. Commun. 47 (2011) 8653–8655.
[6] Y.S. Jang, Y.C. Kang, Phys. Chem. Chem. Phys. 15 (2013) 16437–16441.
[7] T. Stephenson, Z. Li, B. Olsen, D. Mitlin, Energy Environ. Sci. 7 (2014) 209–231.
[8] Y. Li, J.P. Tu, X.H. Huang, H.M. Wu, Y.F. Yuan, Electrochem. Commun. 9 (2007) 49–53.
[9] J.T. Zai, K.X. Wang, Y.Z. Su, X.F. Qian, J.S. Chen, J. Power Sources 196 (2011) 3650–3654.
[10] D. Chen, H. Quan, G.S. Wang, L. Guo, ChemPlusChem 78 (2013) 843–851.
[11] L. Zhang, L. Zhou, H.B. Wu, R. Xu, X.W. Lou, Angew. Chem. Int. Ed. 51 (2012) 7267–7270.
[12] N. Zhang, R. Yi, Z. Wang, R. Shi, H. Wang, G. Qiu, X. Liu, Mater. Chem. Phys. 111 (2008) 13–16.
[13] N. Mahmood, C.Z. Zhang, Y.L. Hou, Small 9 (2013) 1321–1328.
[14] K. Chang, W.X. Chen, Chem. Commun. 47 (2011) 4252–4254.
[15] Q.Q. Zhang, R. Li, M.M. Zhang, B. Zhang, X.L. Gou, Electrochim. Acta 115 (2014) 425–433.
[16] Z. Zhang, C.K. Zhou, L. Huang, X.W. Wang, Y.H. Qu, Y.Q. Lai, J. Li, Electrochim. Acta 114 (2013) 88–94.
[17] Y. Li, J.P. Tu, X.H. Huang, H.M. Wu, Y.F. Yuan, Electrochem. Commun. 9 (2007) 49–53.
[18] G. Huang, T. Chen, Z. Wang, K. Chang, W. Chen, J. Power Sources 235 (2013) 122–128.
[19] Y. Liu, Y. Qiao, W.X. Zhang, Z. Li, X.L. Hu, L.X. Yuan, Y.H. Huang, J. Mater. Chem. 22 (2012) 24026–24033.
[20] S.M. Lee, J.K. Lee, Y.C. Kang, Chem. Asian J. 2 (2013) 590–595.
[21] D. Chen, H. Quan, X. Luo, S. Luo, Scr. Mater. 76 (2014) 1–4.
[22] C. Zhang, Z. Wang, Z. Guo, X.W. Lou, ACS Appl. Mater. Interfaces 4 (2012) 3765–3768.
[23] C. Zhang, H.B. Wu, Z. Guo, X.W. Lou, Electrochem. Commun. 20 (2012) 7–10.
[24] K. Chang, W. Chen, J. Mater. Chem. 21 (2011) 17175–17184.
[25] C.H. Xu, B.H. Xu, Y. Gu, Z.Q. Xiong, J. Sun, X.S. Zhao, Energy Environ. Sci. 6 (2013) 1388–1414.
[26] W. Luo, Y. Xie, C. Wu, F. Zheng, Nanotechnology 19 (2008) 075602.
[27] J. Xiao, X. Wang, X.Q. Yang, S. Xun, G. Liu, P.K. Koech, J. Liu, J.P. Lemmon, Adv. Funct. Mater. 21 (2011) 2840–2846.
[28] H.S. Kim, Y.H. Chung, S.H. Kang, Y.E. Sung, Electrochim. Acta 54 (2009) 3606–3610.
[29] B. Wu, H. Song, J. Zhou, X. Chen, Chem. Commun. 47 (2011) 8653–8655.
[30] Y. Gu, Y. Xu, Y. Wang, ACS Appl. Mater. Interfaces 5 (2013) 801–806.
[31] W. Shi, J. Zhu, X. Rui, X. Cao, C. Chen, H. Zhang, H.H. Hng, Q. Yan, ACS Appl. Mater. Interfaces 4 (2012) 2999–3006.
[32] N. Mahmood, C. Zhang, J. Jiang, F. Liu, Y. Hou, Chem. Eur. J. 19 (2013) 5183–5190.
[33] S.H. Choi, S.J. Boo, J. H Lee, Y.C. Kang, Sci. Rep. 4 (2014) 5755.
[34] K.H. Kim, A. Annamalai, S.H. Park, T.H. Kwon, M.W. Pyeon, M.J. Lee, Electrochim. Acta 76 (2012) 192–200.
[35] S.H. Choi, Y.C. Kang, Chem. Eur. J. 20 (2014) 5835–5841.
[36] J.H. Kim, Y.C. Kang, Nanoscale 6 (2014) 4789–4795.
[37] M.Y. Son, J.H. Kim, Y.C. Kang, Electrochim. Acta 116 (2014) 44–50.
[38] G.D. Park, J.H. Lee, J.K. Lee, Y.C. Kang, Nano Res. 7 (2014) 1738–1748.
[39] G. Zhou, D.W. Wang, X. Shan, N. Li, F. Li, H.M. Cheng, J. Mater. Chem. 22 (2012) 11252–11256.
[40] F. Yu, J. Zhang, Y. Yang, G. Song, J. Power Sources 195 (2010) 6873–6878.
[41] S.W. Han, J.H. Ryu, J. Jeong, D.H. Yoon, J. Alloys Compd. 570 (2013) 144–149.
[42] C.T. Hsieh, I.L. Chen, Y.R. Jiang, J.Y. Lin, Solid State Ionics 201 (2011) 60–67.
[43] S.H. Hong, J.S. Bae, H.J. Ahn, Met. Mater. Int. 14 (2008) 229–232.
[44] F.X. Wu, Z.X. Wang, X.H. Li, H.J. Guo, P. Yue, X.H. Xiong, Z.J. He, Q. Zhang, Electrochim. Acta 78 (2012) 331–339.
[45] D. Li, A. Ito, K. Kobayakawa, H. Noguchi, Y. Sato, J. Power Sources 161 (2006) 1241–1246.
[46] M. Schroeder, S. Glatthaar, H. Geßwein, V. Winkler, M. Bruns, T. Scherer, V.S.K. Chakravadhanula, J.R. Binder, J. Mater. Sci. 48 (2013) 3404–3414.
[47] D. Li, A. Ito, K. Kobayakawa, H. Noguchi, Y. Sato, Electrochim. Acta 52 (2007) 1919–1924.
[48] I. Taniguchi, N. Fukuda, M. Konarova, Powder Technol. 181 (2008) 228–236.
[49] J. Wang, C. Zhang, D. Jin, K. Xie, B. Wei, J. Mater. Chem. A (2015), http://dx.doi.org/10.1039/C5TA02440D.
[50] Y. Ding, J. Du, L. Guo, H. Zhou, H. Yang, F. Wang, Electrochim. Acta 170 (2015) 9–15.
[51] X. Yu, C. Li-yun, H. Jian-feng, L. Jia, F. Jie, Y. Chun-yan, J. Alloys Compd. 549 (2013) 1–5.
[52] X. Li, J. Shen, N. Li, M. Ye, J. Power Sources 282 (2015) 194–201.
[53] T. Wu, F. Tu, S. Liu, S. Zhuang, G. Jin, C. Pan, J. Mater. Sci. 49 (2014) 1861–1867.
[54] Y. Xiao, X. Wang, W. Wang, D. Zhao, M. Cao, ACS Appl. Mater. Interfaces 6 (2014) 2051–2058.
[55] J. Zai, C. Yu, L. Tao, M. Xu, Y. Xiao, B. Li, Q. Han, K. Wang, X. Qian, CrystEngComm 15 (2013) 6663–6671.
[56] L. Tao, J. Zai, K. Wang, H. Zhang, M. Xu, J. Shen, Y. Su, X. Qian, J. Power Sources 202 (2012) 230–235.
[57] Y. Xiao, X. Li, J. Zai, K. Wang, Y. Gong, B. Li, Q. Han, X. Qian, Nano-Micro Lett. 67 (2014) 307–315.
[58] Y. Xiao, J. Zai, X. Li, Y. Gong, B. Li, Q. Han, X. Qian, Nano Energy 6 (2014) 51–58.
[59] Y.N. Ko, S.B. Park, K.Y. Jung, Y.C. Kang, Nano Lett. 13 (2013) 5462–5466.
[60] X.Y. Du, W. He, X.D. Zhang, Y.Z. Yue, H. Liu, X.G. Zhang, D.D. Min, X.X. Ge, Y. Du, J. Mater. Chem. 22 (2012) 5960–5969.